Journal Name

ARTICLE

Combining sonicated cold development and pulsed electrodeposition for high aspect ratio sub-10-nm gap gold dimers for sensing applications in the visible spectrum

Received 00th January 20xx,
Accepted 00th January 20xx

DOI: 10.1039/x0xx00000x

www.rsc.org/

Aaron D. Mueller,[a] Landobasa Y. M. Tobing[a] and Dao Hua Zhang*[a]

Strong interaction between localized surface plasmons and nanoscale objects has led to the development of highly sensitive biochemical sensing in planar metallic nanostructures with sensing performances mainly dependent on the interaction volume and the local electric field. However, the sensitivity and the interaction volume of these planar structures have been limited by the achievable aspect ratios based on the standard lift-off process. We propose a new technique which involves cold sonicated development and pulsed electrodeposition to overcome this limitation, and demonstrate robust gold square dimers with sub-10-nm gaps and gap aspect ratio of ~8. We show that smooth gold surfaces can be achieved by growing the gold film directly on transparent ITO substrate without gold seed layer, and demonstrate significant improvement of Q factors and resonance contrast in electrodeposited dimers compared to dimers fabricated by physical vapor deposition. We demonstrate that the electrodeposited dimers exhibit near 50% higher bulk refractive index sensitivity than their planar counterparts. The technique may be used to grow a variety of metals of arbitrary geometries and spatial arrangements.

Introduction

The ability to fabricate high density arrays of metallic nanostructures has enabled progress in diverse fields including high-density data storage [1,2], localized surface plasmon resonance (LSPR) [3–5], and surface enhanced Raman scattering (SERS) based chemical and bio-sensors [6,7]. It has also proven instrumental in more fundamental research areas such as subwavelength imaging [8] and metamaterials [9]. The strong interaction between surface plasmons and nanoscale objects has led to the development of highly sensitive biochemical sensing at the wavelength bands covering from visible to mid-IR [5,10–13]. The sensitivity depends on the light-matter interaction, which is mostly determined by the surface area of the metal on which (bio-)molecules adhere. Therefore, the sensitivity can be improved by either increasing the lateral size or the height of the resonators. However, increasing resonator size is not effective due to the strong lateral size dependence of plasmonic resonance. In addition to having a red shift in the plasmonic resonance, increasing the size also decreases the pattern density which in turn negatively affects the spectral contrast. On the other hand, increasing the resonator height maintains the pattern density and does not significantly affect the resonance position. Moreover, increasing height also increases the spectral contrast due to enhanced light-matter interaction resulting from a larger surface area.

High aspect ratio metallic nanostructures are thus desired for the above applications. For both research and commercial applications of such structures, it is desirable to have a straightforward and cost-effective fabrication procedure. Several methodologies exist for fabricating 2D and quasi-3D arrays of metallic nanostructures, ranging from subtractive methods, such as focused ion beam (FIB) milling [14], to additive methods based on templates that can be fabricated either by means of self-assembly approaches [15] or lithographic patterning [16,17]. Each templated deposition approach has advantages and disadvantages. Self-assembled monolayers (SAM) allow the formation of a highly ordered hexagonal lattice configuration with high throughput, but at the expense of lack of dimensional control as the sizes are predetermined by those of the nanospheres. In addition, self-assembled monolayers often exhibit uncontrollable domain boundaries. The other more guided self-assembly approach utilizes anodized aluminum oxide (AAO), where a porous template can be defined by means of oxidation of aluminum film. Although the lattice and pore shape can be directed to an extent by pre-anodization patterning using methods such as nanoindentation [18], FIB milling [19], or selective etching [20], AAO templates are constrained by the same lattice and domain issues as the SAM approach.

By contrast, direct template patterning using electron beam lithography (EBL) offers superb dimensional control at the expense of low throughput. While sub-10-nm resolution is required for realizing metallic resonators with strong light-matter interaction capabilities and resonances covering visible spectrum, these dimensions are normally achieved at the

---

[a] School of Electrical and Electronic Engineering, Nanyang Technological University, 50 Nanyang Avenue, S639798. E-mail: edhzhang@ntu.edu.sg

†Electronic Supplementary Information (ESI) available: Additional SEM images with overlaid scale bars denoting measurements, simulations showing resonance blueshift with height increase. See DOI: 10.1039/x0xx00000x

expense of decreased throughput due to the inherent resolution-throughput trade-off. Such a trade-off originates from the attempt to reduce proximity effects in a high contrast EBL process, where the exposed resist is more selectively removed by weak development schemes, such as the use of diluted developer and/or cold development [21–24]. The attempt to overcome this trade-off has been addressed by a cold sonicated development process [25–27], where sonication is introduced during the development step to create interplay between gel-layer formation and removal in partially exposed resist. Using this method, we have achieved a process contrast larger than $\gamma \sim 25$ at an exposure dose much lower than those in reported high contrast EBL processes and have demonstrated the fabrication of planar plasmonic nanostructures with sub-20-nm features [28]. However, the thickness of these planar resonators is constrained by the requirement of ensuring successful lift-off pattern transfer, thereby limiting the metal thickness to a few tens of nanometers. Increasing the aspect ratio is possible with thicker resist, but this is realized at the expense of decreased resolution.

In this work, we address this problem by combining high contrast EBL patterning of the sonicated cold development process with pulsed electrodeposition to realize arrays of metallic resonators with sub-10-nm features and aspect ratio of ~8. We further demonstrate that these dimers exhibit strong resonances in the visible spectrum with Q factors much higher than their planar counterparts. Such geometric and resonance characteristics make them suitable candidates for chemical and bio-sensing substrates, among other applications.

Results and Discussion

Fabrication of square dimer with high aspect ratio gaps

In lift-off pattern transfer, metal is deposited anisotropically through resist with lithographic patterns, followed by resist removal that leaves behind metallic patterns. To ensure successful lift-off transfer, the as-deposited metal film needs to be discontinuous across the patterns. This empirically limits the metal thickness to $\sim$1/3 that of the resist [29]. This is qualitatively different from the electrodeposition process, which enables the growth of metal by filling the lithographic patterns with thickness only limited by the resist thickness. This would translate to $\sim$3x higher aspect ratio than that achievable in a planar fabrication process. Because the cathode (here the substrate) must be conductive, a thin seed layer of the same metal is typically needed prior to electrodeposition. However, in this work the electrodeposition was performed directly onto indium tin oxide- (ITO-) coated glass with the following considerations: The sheet resistance of the ITO glass is chosen to be 20 Ω/□, which is sufficient for electrodeposition without interfering too much with the plasmonic activity of the metal nanostructures. Such a direct electrodeposition also avoids the need to dry etch the gold seed layer, for which the low volatility of gold etch products has been found to be a problem [30]. Finally, in addition to simplifying the fabrication process, this method allows for direct spectral measurements of the nanostructures without the need for post-processing after template removal. DC electrodeposition through a lithographically defined template directly onto ITO has been demonstrated previously [31], but the resulting structures have large lateral features and rough metal surfaces.

In the following, we demonstrate the fabrication of high aspect ratio gold square dimers with gaps in the sub-10-nm regime by combining cold sonicated development and pulsed electrodeposition. The pulsed electrodeposition was based on square wave with 400 ms period and 25% duty cycle (see methods). Square dimers were chosen for their design simplicity and large local electric field across the dimer gaps. In addition, the plasmonic resonance of the square dimers is higher in Q factor compared to that of bowtie nanoantennas, making them suitable candidates for SERS and biosensing substrates [32]. As schematically shown in Figure 1, the dimer is generally characterized in terms of its side lengths (s_x, s_y), gap (g), and height (h). Note that although the dimer design is a square ($s_x = s_y = s$), the actual dimer side lengths may differ due to nonidealities in electrodeposition and EBL proximity effects. In order to prevent strong coupling between adjacent dimers, the periodicity (p) of the dimer array is normalized to $p = 4s$. This periodicity also provides a sufficient signal for measuring the transmission response.

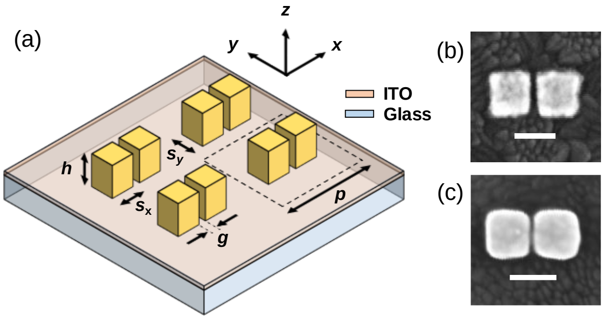

Figure 1 (a) Schematic of the square dimer array on ITO substrate with the unit cell indicated by the dashed square. Top-view SEM micrograph of square dimers with sub-10-nm gaps fabricated by (b) physical vapor deposition and (c) electrodeposition method. The scale bars represent 100 nm.

The fabricated dimers with different side lengths and gaps are presented in Figure 2. The side lengths are designed as s = 60 nm and 80 nm, each of which has gap variations of g= 20 nm, 30 nm, and 40 nm. All dimer structures generally have good pattern fidelity with smooth surface roughness, demonstrating the consistency of our fabrication process. We note an increasing rounding in the dimer at decreasing side length, and that the measured gap appears to be smaller than the designed gap. These are mainly attributed to the intra- and inter-proximity effects during EBL patterning. However, due to the high contrast EBL process based on sonicated cold development, the extent of such proximity effects is limited to a unit cell of the dimer array. This suggests that these proximity effects do not increase with the array footprint, as illustrated by the regularity of the fabricated dimers over a large area in Figure 3.

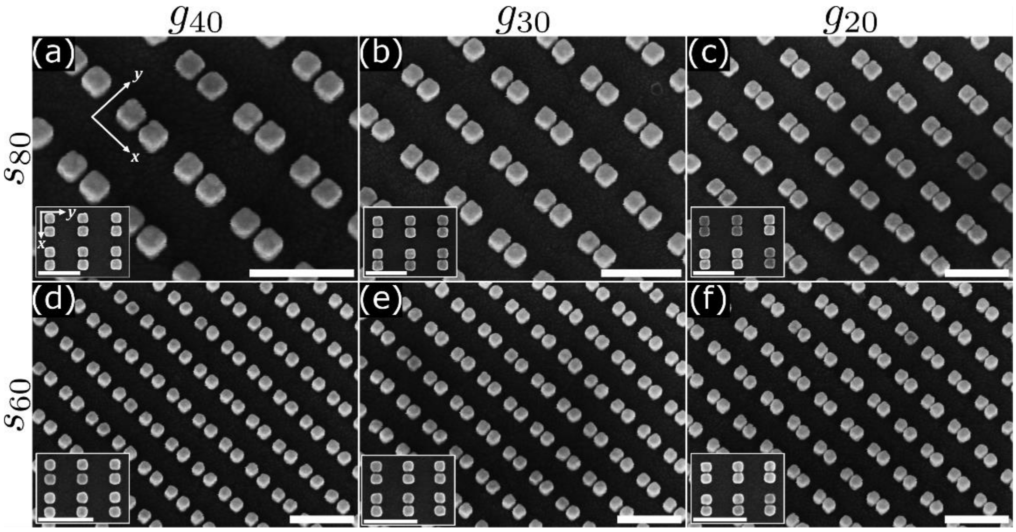

Figure 2 Oblique-incidence SEM images of the fabricated dimer arrays with normal-incidence SEM images inset. (a)-(c) Design square dimension of 80nm with gap decreasing from 40nm to 20nm and (d)-(f) the same as above but with square dimension of 60nm. The inclination angle for the oblique images is 25°. All scale bars are 400 nm.

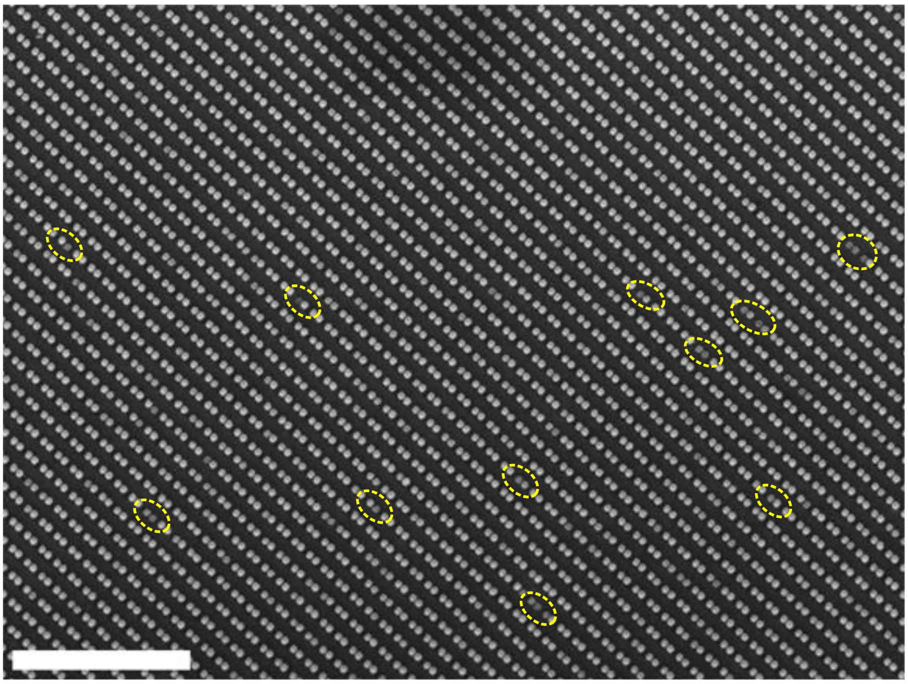

Figure 3 Zoomed out version of the array shown in Fig. 1 (e), with s = 60nm and g =30nm, showing the regularity of the fabricated array. The scale bar represents 2 µm.

Note that some dimers in Figure 3 are shorter than the typical height, as indicated by the dashed yellow circles. This type of defect is likely due to the cessation of growth upon gas (hydrogen) bubble evolution at the top of the structures, prohibiting ion transport to the gold surface, but may also occur during the resist removal step, particularly when it requires sonication which may cause structural fracturing. Due to the nature of the growth mechanisms of electrodeposition and the nanometric dimensions of the template, the final structures exhibit larger lateral dimensions than defined by the template. We summarize the difference between the designed and the measured dimensions in Table 1, where the measurements of the lateral dimensions and height were carried out on normal and oblique incidences SEM micrographs, respectively (see supplementary information).

The sub-10-nm gaps can be achieved for both side lengths at g = 20 nm nominal gap, with average heights larger than 70 nm. For both the s_{60} and s_{80} structures, the final maximum lateral dimensions of the squares were larger than the designed dimensions by slightly over 20 nm. This increase in size is due to the outward lateral pressure of the growing gold structures on the surrounding resist. Due to the pressure from the opposing dimer, the lateral growth in the *x* direction is less than that in the *y* direction by about 2%, 4-5%, and 7% for the dimers with design gaps of 40, 30, and 20 nm, respectively, based on the average measured values. This opposing dimer pressure also keeps the dimer faces straighter on the gap side, particularly for smaller gap size. Figure 4 illustrates the trends in fabricated lateral side length and gap size, normalized to the respective design parameters, with changing gap size, based on the mean data recorded in Table 1.

Table 1 Measured dimensions of dimers, in nm, and aspect ratios

Structure		s_x	s_y	g	h	AR_{s_x}	AR_g
s_{60}	g_{20}	76.7	82.6	8.8	72.6	0.95	8.21
	g_{30}	79.3	83.3	14.4	82.0	1.03	5.68
	g_{40}	80.6	82.2	23.9	74.5	0.93	3.12
s_{80}	g_{20}	96.0	103.6	9.5	78.2	0.82	8.25
	g_{30}	98.5	102.8	16.2	75.3	0.76	4.64
	g_{40}	100.9	102.6	23.1	81.1	0.80	3.51

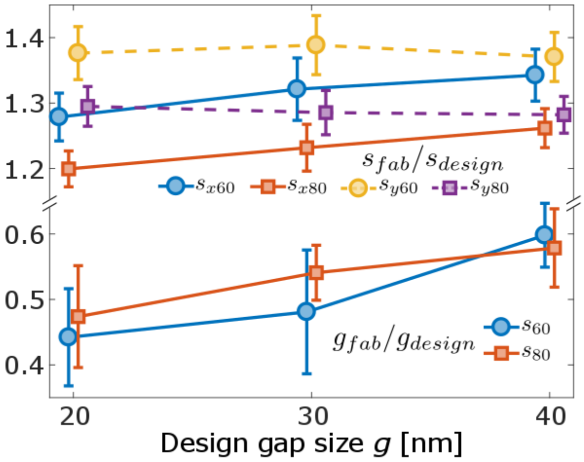

Figure 4 Averages of the normalized measurements with error bars based on the standard deviations, plotted with respect to design gap size, for both the 60nm and 80nm iterations. Above, side length the measurements in the x (s_x) and y (s_y) and directions. Below, the normalized gap measurements. Jitter was added to the abscissa for clearer viewing.

Clearly, both the normalized gap widths and square side lengths in the *x* direction (s_x/s) increase with increasing design gap size, at roughly the same rates. The normalized side lengths s_y/s on the other hand exhibit slightly negative to no correlation with the gap size. This is because increasing the gap size allows more growth in the *x* direction, thus reducing growth in the *y* direction until the growth becomes laterally isotropic.

From the distribution of dimer heights in Figure 5, it can be seen the lower bounds are very close, with the exception of the $s_{80}g_{20}$ and $s_{80}g_{30}$ arrays, in which there were more defects. Additionally, excluding the largest measurement from the $s_{60}g_{30}$ structure, the upper bounds of the height measurements are all similar. The median heights of the arrays parallel the average values, however there doesn't seem to be any trend with respect to side or gap length. This is one intended outcome of the proposed fabrication process: that the final structure height is independent of lateral cross-sectional area.

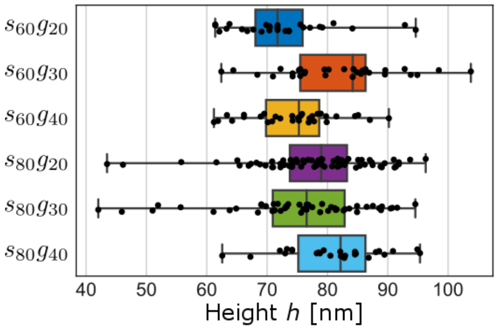

Figure 5 Boxplots showing the distribution of measured dimer heights. Individual data points are also shown, with added jitter. Whiskers are extended to the measured extrema.

We define the aspect ratio as the ratio of height to smallest lateral dimension. The aspect ratios of the side length (AR_{s_x}) and the gap (AR_g) are listed in Table 1. Despite the aspect ratios of the square structures themselves being unremarkable, ranging from 0.76 to 1.03, the aspect ratios of the gaps reached as high as 8.21 and 8.25 for the $s_{60}g_{20}$ and $s_{80}g_{20}$ structures, respectively. The upper limit for the achievable aspect ratio based on sonicated cold development process is ~10 [26], suggesting that further optimization is still possible.

Plasmonic characteristics of gold square dimers

We used a broadband source and hyperspectral imaging system to measure the transmission spectra of the planar and high aspect ratio dimers. As illustrated in Figure 6, which depicts the transmission responses under *x* and *y* polarizations, the plasmonic resonances for the taller dimers exhibit higher *Q* factor and spectral contrast than those of the planar dimers. This is attributed to lower damping loss due to a smoother metal surface in the electrodeposited dimers. We also observed a blue shift of the transverse mode resonance resulting from the increase in dimer height (see supplementary information), where the resonance shifts from 701 nm (682 nm) to 679 nm (623 nm) for resonances under *x* polarization (*y* polarization).

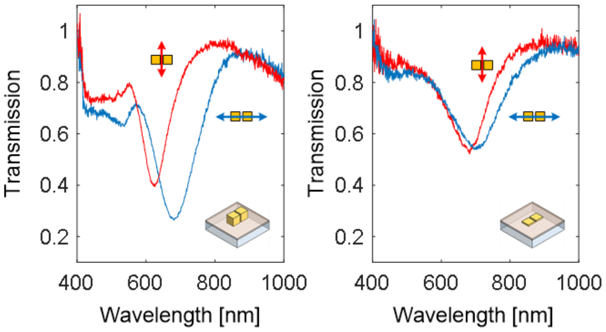

Figure 6 Transmission responses of high aspect ratio (on 20 Ω/□ ITO) and planar (on 50 Ω/□ ITO) square dimer structures (*s* = 80 nm, *g* = 30 nm) under *x* and *y* polarizations.

Figure 7 shows the transmission characteristics of electrodeposited square dimers with varying nominal side lengths and gaps. As expected from the optical properties of dimers, as the incident light is polarized along dimer long axis (*x*-polarization), the resonance progressively red shifts at decreasing gap separation as a result of longitudinal dipolar coupling. The coupling strength increases dramatically at decreasing gap due to the $1/g^3$ dependence in dipolar coupling [33]. This can clearly be seen when the gap is in the sub-10-nm regime (corresponding to the nominal g = 20 nm), where the resonance becomes wider and less pronounced due to the increase in coupling loss. The corresponding *x*-polarized resonance positions at nominal gaps of g = 40 nm, 30 nm, 20 nm are 633.4 nm, 642.4 nm, and 660 nm (for s_{60} structures) and 678.5 nm, 680.4 nm, and 693.7 nm (for s_{80} structures). The resonances along the *y* polarization are invariably shorter than the *x*-polarized resonances and their resonance positions have little dependence on the gap separation. This is attributed to the absence of capacitive interaction between the two gold squares because their dipole oscillations are orthogonal to the dimer gap.

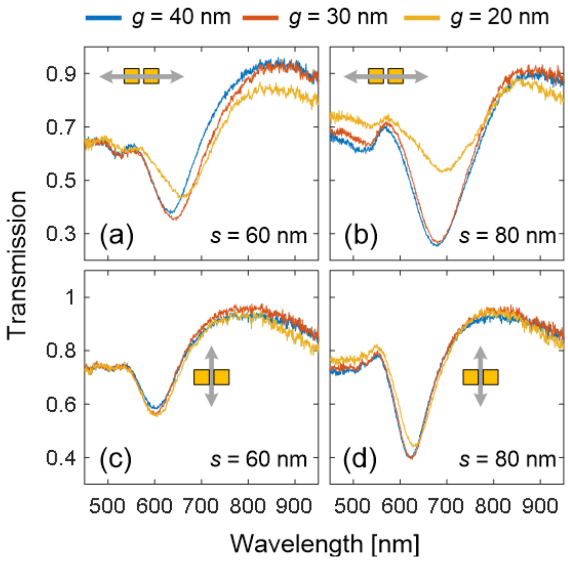

Figure 7 Transmission response of the square dimer structures under *x* and *y* polarizations.

Table 2 summarizes the Q factors of all the dimers considered in this work. As expected from the smoother metal surface, the Q factor for the electrodeposited dimers is higher than their planar counterparts for all combination of sizes and gaps. The Q factors for the *y*-polarized resonances are noticeably higher than those for the *x*-polarized resonance, which is attributed to the absence of coupling loss associated with longitudinal dipolar coupling under *y* polarization. The Q factors for the electrodeposited dimers with sub-10-nm gaps are Q_x~7.62 (s = 60 nm) and Q_x~6.27 (s = 80 nm) under *x* polarizations. This is suitable for light matter interaction at the nanoscale where both high Q factor and high intensity enhancement are simultaneously achieved. More importantly, such pronounced resonances and their strong field enhancements occur within the visible spectrum, which is of practical importance for realizing robust sensing platform based on inexpensive light sources and detectors.

Table 2 Summary of Q factors

Structure		Electrodeposited		Planar	
		Q_x	Q_y	Q_x	Q_y
	g_{20}	7.62	8.85	4.28	6.97
s_{60}	g_{30}	7.60	9.41	6.07	7.02
	g_{40}	8.19	9.23	5.89	6.99
	g_{20}	6.27	8.05	2.75	5.09
s_{80}	g_{30}	6.34	8.82	4.87	5.86
	g_{40}	6.05	8.82	5.03	5.86

Bulk sensing performance

To compare the plasmonic sensing performance of the electrodeposited structures with that of their planar counterparts, we measured the respective transmission spectra of the dimer arrays after spin-coating two resists with two different refractive indices, namely poly(methyl methacrylate) (PMMA) and AZ5214E. Prior to the bulk sensitivity measurements the structures were first cleaned by piranha solution to remove residual organics. We found that this cleaning affected the spectral characteristics of our dimers, where the spectral contrasts after piranha cleaning are observably lower than those of the as-fabricated dimers. The transmission spectra of the electrodeposited and planar $s_{80}g_{40}$ and $s_{80}g_{30}$ arrays are shown in Figure 8 for the three cladding situations.

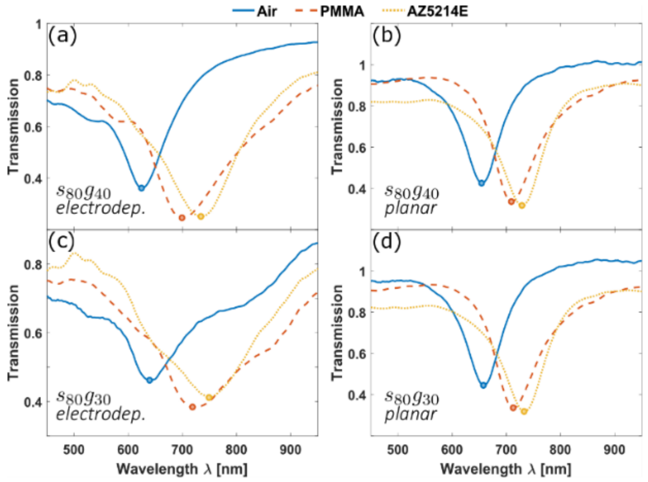

Figure 8 Comparison of electrodeposited deposited and planar dimer transmission spectra in air and in two resists: (a) $s_{80}g_{40}$ electrodeposited array, (b) $s_{80}g_{40}$ planar array, (c) $s_{80}g_{30}$ electrodeposited array, and (d) $s_{80}g_{30}$ planar array. In all spectra, the resonance wavelength is denoted with a circle.

In Figure 9, we use the transmission dip wavelengths, denoted by the circles in Figure 8, along with the refractive indices of air, PMMA, and AZ5214E to plot the wavelength as a function of cladding index for each of the two dimer arrays. The refractive indices of PMMA and AZ5214E are taken from reference 33 and found using the Cauchy equation with parameters given on the manufacturer's data sheet, respectively (see supplementary information). Assuming $\lambda =$ 600 nm, representative of the operation wavelength of interest for visible sensing characterization, the refractive indices are $n_{PMMA} = 1.4901$ and $n_{AZ} = 1.6370$.

The resonance wavelengths follow linear relationships, represented by the dashed lines of best fit. The refractive index sensitivities (S) are given by the slopes of the lines, in nanometers per refractive index unit (nm/RIU). The sensitivities for the $s_{80}g_{40}$ dimers are 115.6 nm/RIU (planar) and 167.2 nm/RIU (electrodeposited), while those for the $s_{80}g_{30}$ are 116.6 nm/RIU (planar) and 169.6 nm/RIU (electrodeposited). These represent increases in the sensitivities of the electrodeposited (h~75—80 nm) over the planar (h~30 nm) arrays of about 45% in both cases. These sensitivities are close to those of colloidally-prepared gold nanorods for the same resonance wavelength range, which have the best surface morphology owing to their crystallinity [35,36]. The figure of merit (FOM) for refractometric sensors is defined as $FoM = S/FWHM$, where *FWHM* is the full-width at half-maximum linewidth of the resonance in air. Using $Q = \lambda_R/FWHM$ and the $S \propto \lambda_R$ dependence of sensitivity on resonance wavelength [37], we can arrive at the following conclusion $FoM \propto Q$ [38]. Taking Q factors for $s_{80}g_{40}$ and $s_{80}g_{30}$ from Table 2, it can be concluded that the *FoMs* increase by factors of 1.3 and 1.2, respectively, in addition to having higher sensitivity with lower starting λ_R. Since $Q \propto \lambda_R$, we can infer that the increase in Q for the electrodeposited structures is due to the higher quality of the gold.

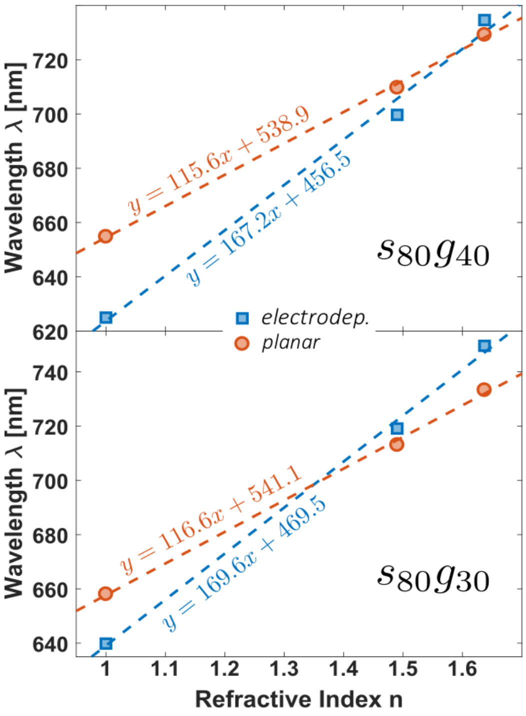

Figure 9 Transmission dip minima plotted against cladding refractive index for the two dimer arrays. The regression lines for the points are also shown.

Conclusions

We have demonstrated a novel process for fabricating metallic nanostructures on an ITO-coated substrate by combining electron beam lithography using a sonicated cold development process with pulsed electrodeposition. EBL allows for precise control of template size, shape, and position, while sonicated cold development ensures near vertical sidewalls at a lower exposure dose. Due to the nature of the templated electrodeposition growth in a soft resist, the metal structures have more rounded features and are laterally larger than the lithographically defined template. Locating structures in close proximity, as is the case with the fabricated dimers, enables the consistent fabrication sub-10-nm gaps. Among dimer arrays presented in this paper, at average heights of 72.6 and 78.2 nm, respectively, the $s_{60}g_{20}$ and $s_{80}g_{20}$ dimer arrays achieved average gap aspect ratios of over 8. Because the height attainable with electrodeposition is dependent only on the height of the resist template, it is possible to use the demonstrated technique to grow much taller structures and achieve higher aspect ratios. Compared to more planar dimers with gold deposited via e-beam evaporation and lift-off, the SEM images of the electrodeposited structures indicate smoother gold film. Though increased height is also a factor, this is also evidenced by the comparatively higher Q factors of the resonance dips in the transmission spectra. These considerations make the electrodeposited structures more suitable for applications in biological and chemical sensing, among others. Furthermore, because of the direct deposition onto the ITO, the need to both deposit and subsequently remove a metal seed layer, at the possible expense of adversely affecting structural integrity, are eliminated.

Experimental

Nanopatterning

The EBL patterning was carried out by Raith e_LiNE system on 120 nm thick ZEP520A e-beam resist based on 20 keV energy and 30 pA beam current. For higher pattern fidelity, the square dimers were written as a series of single pixel lines as opposed to areal exposure. The line exposure was done at 300 pC/cm dose at 2 nm step size. The single pixel lines are separated by 10 nm, which is the intrinsic linewidth of a single dot exposure. Several iterations of square dimer arrays of footprint 10µm by 10µm were written. Each iteration was designed to have a square side length of 60nm or 80nm, and a gap distance of 20nm, 30nm, or 40nm, for a total of six arrays. In all cases, the periodicity was set to four times the square side length. The sample was then developed in a mixture of *n*-amyl acetate and isopropanol (2:1) using a sonicated cold development process with 5s pre-sonication time, 10s sonication time, and 20s post-sonication time. This process has been reported to exhibit high verticality (with <5° sidewall angle) [27] and aspect ratio of ~10 [26], making it suitable for growing square dimers with sub-10-nm gaps. For planar square dimer fabrication, 30 nm thick gold was physically deposited by an e-beam evaporator (Edwards 306) at 0.05 nm/s rate using 2 nm thick titanium as adhesion layer, followed by a lift-off process in N-methylpyrrolidine based solvent (Remover PG, MicroChem Corp) for 10 mins at room temperature.

Electrodeposition

For the growth of the gold dimer structures, the patterned sample and a bare ITO glass were placed in a holder exposing their conductive ITO surfaces to the electroplating solution. The purpose of using bare ITO glass as a dummy sample is to permit the control of current density which is independent of nanopattern area. It was previously found that good results could be achieved by providing a current density of 3 mA/cm2 to the sample. Based on the areas of the patterns alone, the current needs to be in picoampere range to achieve the desired current density. However, by having bare ITO glass with 0.28 cm^2 opening area (i.e. the area of the 6 mm-diameter silicone O-ring used in the electroplating holder), and assuming the dummy area is much larger than that of the nanopatterns ($A_{dummy} \gg A_{nano}$), the required current was found to be 0.85 mA. Based on this method, the plating current density has been varied to as low as 1 mA/cm2 without much difficulty. The electroplating was done in a commercially available mixture based on potassium aurocyanide [$KAu(CN)_2$] at room temperature. The electroplating was done using both DC and pulsed current schemes. The latter is found to exhibit higher uniformity and smaller surface roughness. The pulsed plating was done with a Keithley 2400 SourceMeter at 0.85 mA current in square waveform of 400 ms period and 25% duty cycle. A total of 10 pulses were used in the plating, corresponding to a total "ON" time of 1s. The pulsed current waveform was programmed through the RS232 interface using SCPI and MATLAB. Following electrodeposition, the sample was rinsed in DI water. The resist template was then removed using N-methylpyrrolidine, followed by rinsing in isopropanol.

SEM measurements

SEM images were obtained using the EBL system at 10 keV. Measurements of the fabricated dimers were performed using Inkscape software. Lateral and vertical measurement bars on the SEM images, as well as the dimer height calculation method, can be found in the Supplementary Information.

Transmission measurements

The square dimers were characterized by the Cytoviva hyperspectral imaging system. The halogen lamp was focused by a condenser into the sample and the transmission signals were collected by 10x objective lens (NA 0.3) under bright field geometry. The signals were directed to the transmission grating and CCD sensor, and the piezo stage was scanned in order to get the transmission image. The transmission for a particular dimer array was obtained from the pixels corresponding to the structure, followed by normalization with respect to the signals from the bare substrate.

Conflicts of interest

There are no conflicts to declare.

Acknowledgements

This work was supported by the Ministry of Education (RG86/13), the Economic Development Board (NRF2013SAS-SRP001-019), Singapore; and the Asian Office of Aerospace Research and Development (FA2386-17-1-0039).

Notes and references

1 J. Wi, H. Lee, K. Lim, S. Nam, H. Kim, S. Park, J. J. Lee, C. D. Hong, S. Jin and K. Kim, Small, 2008, 4, 2118–2122.
2 T. R. Albrecht, D. Bedau, E. Dobisz, H. Gao, M. Grobis, O. Hellwig, D. Kercher, J. Lille, E. Marinero, K. Patel, R. Ruiz, M. E. Schabes, L. Wan, D. Weller and T.-W. Wu, IEEE Trans. Magn., 2013, 49, 773–778.
3 X. Huang, S. Neretina and M. a. El-Sayed, Adv. Mater., 2009, 21, 4880–4910.
4 A. V. Kabashin, P. Evans, S. Pastkovsky, W. Hendren, G. A. Wurtz, R. Atkinson, R. Pollard, V. A. Podolskiy and A. V. Zayats, Nat. Mater., 2009, 8, 867–871.
5 A. M. Soehartono, A. D. Mueller, L. Y. M. Tobing, K. K. Chan, D. H. Zhang and K.-T. Yong, Nanotechnology, 2017, 28, 405305.
6 Q. Yu, S. Braswell, B. Christin, J. Xu, P. M. Wallace, H. Gong and D. Kaminsky, Nanotechnology, 2010, 21, 355301.
7 J. D. Caldwell, O. Glembocki, F. J. Bezares, N. D. Bassim, R. W. Rendell, M. Feygelson, M. Ukaegbu, R. Kasica, L. Shirey and C. Hosten, ACS Nano, 2011, 5, 4046–4055.
8 A. Ono, J. Kato and S. Kawata, Phys. Rev. Lett., 2005, 95, 267407.
9 J. Elser, R. Wangberg, V. a. Podolskiy and E. E. Narimanov, Appl. Phys. Lett., 2006, 89, 261102.
10 A. E. Cetin, D. Etezadi, B. C. Galarreta, M. P. Busson, Y. Eksioglu and H. Altug, ACS Photonics, 2015, 2, 1167–1174.
11 A. E. Cetin, D. Etezadi and H. Altug, Adv. Opt. Mater., 2014, 2, 866–872.
12 A. W. Clark, A. Glidle, D. R. S. Cumming and J. M. Cooper, J. Am. Chem. Soc., 2009, 131, 17615–17619.
13 Y. Chen and H. Ming, Photonic Sensors, 2012, 2, 37–49.
14 P. Luches, A. di Bona, S. F. Contri, G. C. Gazzadi, P. Vavassori, F. Albertini, F. Casoli, L. Nasi, S. Fabbrici and S. Valeri, Acta Phys. Pol. A, 2007, 112, 1297–1312.
15 S. J. Barcelo, S. Lam, G. A. Gibson, X. Sheng and D. Henze, in Proc. SPIE 8323, Alternative Lithographic Technologies IV, 2012, p. 83232L.
16 B. Päivänranta, H. Merbold, R. Giannini, L. Büchi, S. Gorelick, C. David, J. F. Löffler, T. Feurer and Y. Ekinci, ACS Nano, 2011, 5, 6374–6382.
17 L. Y. M. Tobing, Y. Luo, K. S. Low, D. Zhang and D. H. Zhang, Adv. Opt. Mater., 2016, 4, 1047–1052.
18 H. Masuda, K. Yasui, Y. Sakamoto, M. Nakao, T. Tamamura and K. Nishio, Jpn. J. Appl. Phys., 2001, 40, L1267–L1269.
19 B. Chen, K. Lu and Z. Tian, Langmuir, 2010, 27, 800–808.
20 J. T. Smith, Q. Hang, A. D. Franklin, D. B. Janes, and T. D. Sands, Appl. Phys. Lett., 2008, 93, 43108.
21 L. E. Ocola and A. Stein, J. Vac. Sci. Technol. B Microelectron. Nanom. Struct., 2006, 24, 3061.
22 W. Hu, K. Sarveswaran, M. Lieberman, G. H. Bernstein and I. Introduction, J. Vac. Sci. Technol. B Microelectron. Nanom. Struct., 2004, 22, 1711–1716.
23 M. Yan, S. Choi, K. R. V. Subramanian and I. Adesida, J. Vac. Sci. Technol. B Microelectron. Nanom. Struct., 2008, 26, 2306.

24 B. Cord, J. Lutkenhaus and K. K. Berggren, J. Vac. Sci. Technol. B Microelectron. Nanom. Struct., 2007, 25, 2013.

25 L. Y. M. Tobing, L. Tjahjana and D. H. Zhang, J. Vac. Sci. Technol. B Microelectron. Nanom. Struct., 2012, 30, 51601.

26 L. Y. M. Tobing, L. Tjahjana and D. H. Zhang, Nanotechnology, 2013, 24, 75303.

27 L. Y. M. Tobing, L. Tjahjana and D. H. Zhang, IEEE Trans. Nanotechnol., 2014, 13, 496–501.

28 L. Y. M. Tobing and D. H. Zhang, eds. C. K. Hohle and R. Gronheid, International Society for Optics and Photonics, 2017, vol. 10146, p. 101461Q.

29 Cui Z. Nanofabrication Principles, Capabilities, and Limits. Springer; 2008.

30 T. A. Green, Gold Bull., 2014, 47, 205–216.

31 V. Giorgis, P. Zilio, M. Massari, G. Ruffato, G. Zacco and F. Romanato, Microelectron. Eng., 2014, 127, 68–71.

32 E. Hao and G. C. Schatz, J. Chem. Phys., 2004, 120, 357–366.

33 Liu N, Giessen H. Coupling Effects in Optical Metamaterials. Angew Chemie Int Ed. 2010 Dec;49(51):9838–52.

34 Polyanskiy MN. Refractive index database.

35 Zalyubovskiy SJ, Bogdanova M, Deinega A, Lozovik Y, Pris AD, An KH, et al. Theoretical limit of localized surface plasmon resonance sensitivity to local refractive index change and its comparison to conventional surface plasmon resonance sensor. J Opt Soc Am A. 2012;29(6):994–1002.

36 Mayer KM, Lee S, Liao H, Rostro BC, Fuentes A, Scully PT, et al. A label-free immunoassay based upon localized surface plasmon resonance of gold nanorods. ACS Nano. 2008;2(4):687–92.

37 Tobing LYM, Tjahjana L, Zhang DH, Zhang Q, Xiong Q. Deep subwavelength fourfold rotationally symmetric split-ring-resonator metamaterials for highly sensitive and robust biosensing platform. Sci Rep. 2013;3:2437.

38 Tobing LYM, Goh GY, Mueller AD, Ke L, Luo Y, Zhang DH. Polarization invariant plasmonic nanostructures for sensing applications. Sci Rep. 2017;7(1):1–14.